Hodograph Variability within Analytically Modeled, Synoptic-Scale, Baroclinic Systems

PETER C. BANACOS

NOAA/NWS/NCEP Storm Prediction Center, Norman, Oklahoma

HOWARD B. BLUESTEIN

School of Meteorology, University of Oklahoma, Norman, Oklahoma

(Manuscript received 13 August 2003, in final form 12 December 2003)

ABSTRACT

Although the relationship between the behavior of convective storms and their environmental vertical wind shear has been examined using proximity soundings and idealized numerical modeling experiments, the manner in which the vertical shear profiles, as visualized by hodographs, is regulated by the larger-scale baroclinic wave structure has not been considered in detail. To examine this synoptic-scale dependence, a relatively simple, analytic model for baroclinic systems in midlatitudes having exact solutions for a frictionless, quasigeostrophic atmosphere is employed. The analytical model consists of a checkerboard of high and low pressure areas at 1000 mb, hydrostatically modulated above by a mean meridional temperature gradient and a checkerboard of warm and cold centers at 1000 mb. Aloft, the model atmosphere consists of a zonally oriented wave train. This approach allows a systematic examination of the dependence of hodographs on the following five synoptic-scale parameters included in the model: 1) mean meridional temperature gradient, 2) system wavelength, 3) phase lag between the height and temperature fields at 1000 mb, 4) magnitude of the temperature perturbation associated with the checkerboard of warm and cold centers at 1000 mb, and 5) magnitude of the 1000-mb height perturbation.

It is seen that the phase lag between the height and temperature fields and the system wavelength have the greatest quantitative influence on the relative contribution of the ageostrophic wind component to the total wind. These two parameters are associated with significant clockwise curvature with height in the hodograph of the total wind, particularly if the deep-layer ageostrophic wind shear is oriented perpendicular and to the right of the geostrophic shear. Hodograph curvature, however, is not ubiquitous in the model, and despite the model's simplicity, likely speaks to the importance of features departing from the model, mesoscale variability, and boundary layer friction in enhancing hodograph curvature.

1. Introduction

Observational (e.g., Maddox 1976; Bluestein and Jain 1985; Rasmussen and Straka 1998) and numerical (e.g., Weisman and Klemp 1982, 1984; Brooks et al. 1994; Bluestein and Weisman 2000) studies have shown that relatively minor changes in the vertical shear profile can have a strong modulating influence on the ''mode'' of deep moist convection (i.e., the favored organizational structure of convective storms or systems) in conjunction with other physical factors [the most prominent being the magnitude and vertical distribution of potential buoyancy, and the nature and magnitude of the background vertical-motion mechanism(s)]. These studies, however, have not explored how synoptic-scale baroclinic wave structures locally modulate the vertical wind profile, which can affect the organization of mesoscale precipitation. Owing to the frequent connection between deep moist convection and synoptic-scale baroclinic waves aloft (Macdonald 1976; Glickman et al. 1977), a relatively simple analytic model is employed to associate the local shear profile with parameters that describe the character of the synoptic-scale baroclinic wave. A hodograph climatology, developed relative to synoptic-scale cyclone and anticyclone centers over a 37-yr period (Banacos 1999; Bluestein and Banacos 2002), serves as a guide in assessing the applicability of the analytically generated model hodographs.

This paper is organized as follows: Section 2 describes aspects of the analytic model relevant to the derivation of the geostrophic and ageostrophic wind components. Section 3 presents an analysis of hodograph shape for varied configurations of the synoptic-scale baroclinic waves. Last, section 4 provides a concluding discussion and suggestions for future work.

2. Model description and wind field

An analytic model developed by Sanders (1971), which has exact solutions for a frictionless, quasigeo-

Corresponding author address: Peter C. Banacos, Storm Prediction Center, 1313 Halley Circle, Norman, OK 73069.
E-mail: peter.banacos@noaa.gov

strophic (QG) atmosphere, is used to vary systematically the configuration of synoptic-scale baroclinic waves. We begin with a description of the model as it relates to the wind structure [the reader is referred to Sanders (1971) and Bluestein (1993) for a more detailed description of the model].

a. Thermodynamic structure

A simple quasi-horizontal distribution of geopotential (Φ, where $\Phi = gz$) at 1000 mb is given by the following:

$$\Phi(x, y, p = 1000 \text{ mb}) = \hat{\Phi}_0 \cos\frac{2\pi}{L}(x + \lambda) \cos\frac{2\pi}{L}y, \quad (1)$$

where $\hat{\Phi}_0$ is the surface geopotential perturbation, L is the system wavelength (which is isotropic), and λ controls the phase lag of the 1000-mb geopotential field relative to the temperature field; x and y are independent variables representing the east–west and north–south directions, respectively, with positive values of x (y) pointing to the east (north).

The three-dimensional temperature distribution is specified as

$$T(x, y, p) = T_m(p) - \left(1 - \alpha \ln\frac{1000}{p}\right) \times \left(ay + \hat{T} \cos\frac{2\pi}{L}x \cos\frac{2\pi}{L}y\right), \quad (2)$$

where T_m is level-mean temperature, α is a parameter controlling tropopause height (set here to 250 mb), p is pressure expressed in millibars, a is the mean meridional temperature gradient, and $\hat{T}$ is the temperature perturbation associated with the baroclinic waves. The *U.S. Standard Atmosphere, 1976* (COESA 1976) was used initially to define $T_m(p)$ for this experiment. However, owing to the availability of climatological information in the vicinity of cyclones and anticyclones based on previous observational work (Bluestein and Banacos 2002), and our particular interest in the background environment of cyclones when convective storms are most frequent, the mean 0000 UTC cyclone temperature and geopotential profiles within 900 km of surface cyclone centers were used to define these variables in Sanders' model. The model parameters are based on the mean of 44 510 soundings (Table 1). The relatively high static stability in the 950–800-mb layer results in smaller values of height tendency and isallohypsic wind through that layer than is observed when the U.S. Standard Atmosphere is employed. We expect that generally the isallohypsic wind is larger for smaller values of stability based on this result and vertical continuity considerations (i.e., vertical motion is lessened for the same degree of forcing at higher values of static stability according to the QG omega equation). Strong(er) isallohypsic contributions to the boundary layer flow would be expected with steep(er) lapse rates.

TABLE 1. Level-mean temperature (T_m), level-mean geopotential (Φ_m), and the dimensionless stability parameter (γ), listed in 50-mb increments as used in Sanders' analytic model. Parameters based on 0000 UTC rawinsonde data within 900 km of a composite extratropical cyclone (N = 44 510) constructed by Bluestein and Banacos (2002).

p (mb)	T_m(K)	Φ_m (m^2 s^{-2})	γ
1000	283.0	688.9	0.0963
950	281.0	4510.0	0.1927
900	279.9	8857.2	0.2265
850	278.7	13 461.3	0.2038
800	277.1	18 327.0	0.1578
750	274.4	23 443.6	0.1276
700	271.3	28 860.0	0.1171
650	267.9	34 593.0	0.1102
600	264.0	40 717.0	0.0997
550	259.7	47 246.8	0.0945
500	254.9	54 304.7	0.0861
450	249.5	61 910.5	0.0805
400	243.5	70 269.9	0.0767
350	236.8	79 482.9	0.0822
300	229.7	89 786.6	0.1076
250	223.3	101 629.9	0.1653
200	319.3	115 782.1	0.2349
150	217.3	133 801.4	0.2506

For simplicity, the model's lowest level at 1000 mb is taken as the surface of the earth. Friction is not incorporated into the model, for both simplicity and to isolate the effects of baroclinic wave structure on the shape of the hodograph.

The multiplying factor $[1 - \alpha \ln(1000/p)]$ allows for the magnitude of the quasi-horizontal temperature variation to decrease with height, and for the sign of the temperature gradient to reverse at the model tropopause. In the Sanders' model, the height of the tropopause does not vary as it does in the real atmosphere. Since the tropopause in the real atmosphere is lower over cyclones than it is over anticyclones, the model wind field near the tropopause could be in error accordingly. Both the Φ and T fields take the form of an infinite checkerboard of high and low and cold and warm perturbation centers.

Using (1) and the assumption that the atmosphere is hydrostatic, the three-dimensional field of geopotential can be found by upward integration of the hypsometric equation,

$$\partial\Phi = -RT\partial \ln p. \quad (3)$$

As shown by Bluestein (1993), integration yields

$$\Phi(x, y, p) = \Phi_m(p) + \hat{\Phi}_0 \cos\frac{2\pi}{L}(x + \lambda) \cos\frac{2\pi y}{L} + R\left(ay + \hat{T} \cos\frac{2\pi x}{L} \cos\frac{2\pi y}{L}\right) \times \left[\ln\frac{p}{1000} + \frac{\alpha}{2}\left(\ln\frac{p}{1000}\right)^2\right], \quad (4)$$

where $\Phi_m(p)$ is a vertical function representing mean geopotential at a given pressure level, and R is the gas constant for dry air. The level-mean geopotential is determined hydrostatically by logarithmic integration of the level-mean temperature function as follows:

$$\Phi_m(p) = -R \int_{p=1000\text{ mb}}^{p} T_m(p') \frac{dp'}{p'}. \quad (5)$$

Although the model equations use p as the vertical coordinate, wind information is interpolated to constant height levels with respect to height above ground level (AGL), consistent with convention for plotting of hodographs.

In addition to the background vertical temperature profile, $T_m(p)$, background values of γ, an environmental lapse rate defined as a function of pressure, are computed using the following:

$$\gamma(p) = \kappa - p\frac{\partial \ln T_m}{\partial p}. \quad (6)$$

This function is used to determine the static stability parameter, which is necessary to solve the QG height tendency and omega equations. Values of $\gamma(p)$ are given in Table 1 for specific data in the vicinity of cyclones at 0000 UTC, as described earlier, and in Fig. 1 for both cyclones and anticyclones (for comparison) at 0000 UTC, and for a *U.S. Standard Atmosphere.*

b. Determination of model geostrophic and ageostrophic winds

The geostrophic wind ($\mathbf{v}_g$) in pressure coordinates is defined as (Bluestein 1992)

$$\mathbf{v}_g = u_g\mathbf{i} + v_g\mathbf{j} = \frac{1}{f}\mathbf{k} \times \nabla_p\Phi, \quad (7)$$

where f is the Coriolis parameter, defined as $f = 2\Omega \sin\phi$ (Ω is the earth's angular velocity, and ϕ is the latitude). For all configurations presented here, the domain was centered in the north–south direction at 40°N. Since f varies with latitude, we employ the β-plane approximation in order to incorporate the advection of earth's vorticity:

$$f = f_0 + \beta y, \quad (8)$$

where f_0 represents a mean value of the Coriolis parameter for the domain (taken to be 9.374×10^{-5} s^{-1}, the value at 40°N latitude), and β is defined as df/dy (the effect of which is shown later in Fig. 3b).

Expanding on the analysis of Sanders (1971), the three-dimensional function for Φ given in (4) was differentiated to determine analytically the geostrophic wind field. The resultant component equations are

$$u_g = -\frac{1}{f}\Bigg\{-k\hat{\Phi}_0 \cos k(x + \lambda) \sin(ky) + R[a - k\hat{T} \cos(kx) \sin(ky)] \times \left[\ln\left(\frac{p}{1000}\right) + \frac{\alpha}{2}\left(\ln\frac{p}{1000}\right)^2\right]\Bigg\}, \quad (9)$$

$$v_g = \frac{1}{f}\Bigg\{-k\hat{\Phi}_0 \sin k(x + \lambda) \cos(ky) + R[-k\hat{T} \sin(kx) \cos(ky)] \times \left[\ln\left(\frac{p}{1000}\right) + \frac{\alpha}{2}\left(\ln\frac{p}{1000}\right)^2\right]\Bigg\}, \quad (10)$$

where k is the horizontal wavenumber, defined as $k = 2\pi/L$.

The ageostrophic wind is related to the parcel acceleration and is somewhat more complicated to determine. The parcel acceleration in a QG atmosphere is given by

$$\frac{D\mathbf{v}}{Dt} = \frac{D_g\mathbf{v}_g}{Dt} = \frac{\partial \mathbf{v}_g}{\partial t} + (\mathbf{v}_g \cdot \nabla_p)\mathbf{v}_g. \quad (11)$$

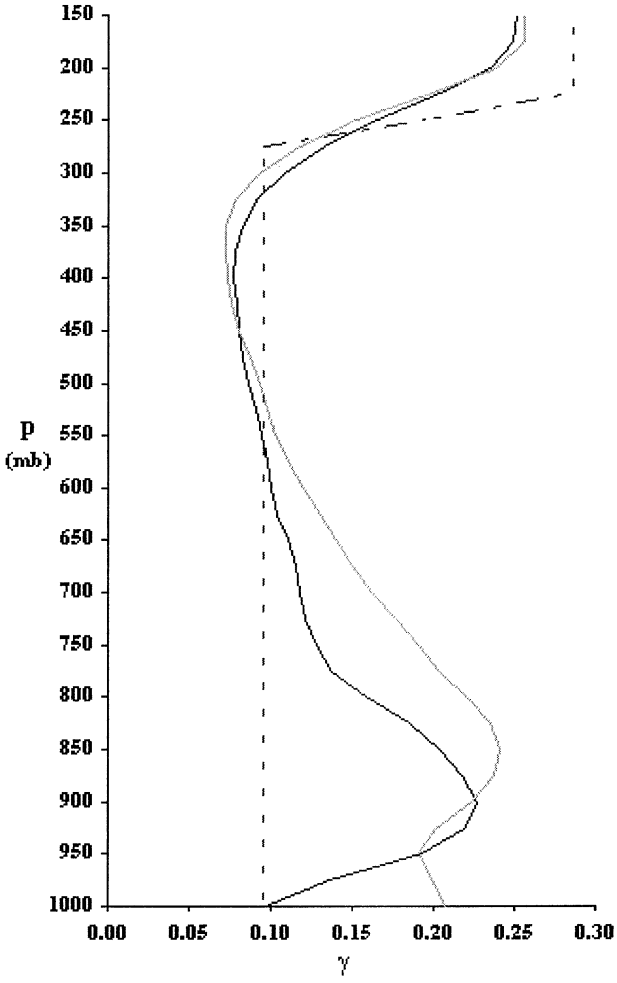

FIG. 1. Vertical profile of dimensionless parameter γ based on the climatological temperature profile of Bluestein and Banacos (2002) surrounding cyclones (black line) and anticyclones (gray line) at 0000 UTC, as well as a vertical profile for the *U.S. Standard Atmosphere* (dashed line).

The QG parcel acceleration involves the time rate of change of the geostrophic wind (first term on rhs), and the geostrophic advection of geostrophic momentum (second term on rhs). The vertical advection of geostrophic momentum and other advections due to the ageostrophic part of the wind are not part of the QG formulation. The ageostrophic wind in a QG atmosphere is defined as (Bluestein 1992)

$$\mathbf{v}_a = \frac{1}{f}\mathbf{k} \times \frac{D\mathbf{v}}{Dt} = \frac{1}{f}\mathbf{k} \times \left[\frac{\partial \mathbf{v}_g}{\partial t} + (\mathbf{v}_g \cdot \nabla_p)\mathbf{v}_g\right]. \quad (12)$$

Therefore, in the Northern Hemisphere, the ageostrophic wind vector is directed perpendicular and to the left of the parcel acceleration. Using pressure as the vertical coordinate, the time tendency of the geostrophic wind is related to the local gradient in geopotential height tendency [as shown in (13)], and therefore the first term on the right-hand side of (12) is often referred to as the isallohypsic contribution. The second term on the right-hand side of (12) is the advection of the geostrophic wind by itself and is frequently referred to as the inertial-advective component of the ageostrophic wind. The inertial-advective contribution becomes dominant for relatively large magnitudes of geostrophic wind in strongly curved flow, and its magnitude is typically greatest in the upper troposphere. It is not always simple to estimate qualitatively how the ageostrophic wind is directed in the free atmosphere since the contributing terms often act opposite to one another. This aspect of the ageostrophic wind is discussed further in section 3.

Taking the derivative with respect to time of (7) and changing the order of differentiation relates the time tendency of the geostrophic wind to the quasi-horizontal gradient in height tendency, χ, as follows:

$$\frac{\partial \mathbf{v}_g}{\partial t} = \frac{1}{f}\mathbf{k} \times (\nabla_p \chi), \quad (13)$$

where the height tendency is defined as $\chi = \partial\Phi/\partial t$. The resulting component equations for the isallohypsic wind are

$$u_a = -\frac{1}{f}\frac{\partial v_g}{\partial t}, \quad (14a)$$

$$v_a = \frac{1}{f}\frac{\partial u_g}{\partial t}. \quad (14b)$$

The height tendency can be determined analytically in the model using the QG form of the vorticity equation:

$$\frac{\partial \zeta_g}{\partial t} = -\mathbf{v} \cdot \nabla_p(\zeta_g + f) - f\left(\frac{\partial u}{\partial x} + \frac{\partial v}{\partial y}\right), \quad (15)$$

where ζ_g is the geostrophic vorticity. Making use of the equation of continuity and the definition of the geostrophic wind in $\zeta_g = (\partial v_g/\partial x) - (\partial u_g/\partial y) = 1/f_0(\nabla^2\Phi)$ yields

$$\nabla_p^2 \chi = f_0[-\mathbf{v}_g \cdot \nabla_p(\zeta_g + f)] + f_0^2\left(\frac{\partial \omega}{\partial p}\right). \quad (16)$$

In conjunction with analytic solutions to the QG omega equation, solutions to χ can be found. These solutions, which are cumbersome, are given by Sanders (1971) and by Bluestein (1993).

The inertial-advective contribution to the QG form of the ageostrophic wind is determined more straightforwardly, since it involves only combinations of the geostrophic wind and its horizontal derivatives. The QG inertial-advective contribution to the ageostrophic wind can be expressed as

$$(\mathbf{v}_g \cdot \nabla_p)\mathbf{v}_g = u_g\frac{\partial \mathbf{v}_g}{\partial x} + v_g\frac{\partial \mathbf{v}_g}{\partial y}. \quad (17)$$

The component equations for the inertial-advective wind are as follows:

$$u_a = -\frac{1}{f}\left(u_g\frac{\partial v_g}{\partial x} + v_g\frac{\partial v_g}{\partial y}\right), \quad (18a)$$

$$v_a = \frac{1}{f}\left(u_g\frac{\partial u_g}{\partial x} + v_g\frac{\partial u_g}{\partial y}\right). \quad (18b)$$

The total ageostrophic wind components are therefore

$$u_a = -\frac{1}{f}\left(\frac{\partial v_g}{\partial t} + u_g\frac{\partial v_g}{\partial x} + v_g\frac{\partial v_g}{\partial y}\right), \quad (19a)$$

$$v_a = \frac{1}{f}\left(\frac{\partial u_g}{\partial t} + u_g\frac{\partial u_g}{\partial x} + v_g\frac{\partial u_g}{\partial y}\right). \quad (19b)$$

3. Methodology and hodograph analysis

a. Overview of parameter space

We are interested primarily in the effects of the following five variables on the baroclinic wave structure: 1) mean meridional temperature gradient (a), 2) system wavelength (L), 3) phase lag (λ), 4) magnitude of the temperature perturbation ($\hat{T}$), and 5) magnitude of the surface height perturbation ($\hat{\Phi}_0$). The relationship of these variables to the 3D analytic model structure was shown in the previous section. Each of these variables is varied independently of the others and forms a ''control'' simulation over a parameter space consistent with values commonly observed in midlatitude pressure systems. For this portion of the study, nine values of each parameter were analyzed at three points located one-sixteenth of a wavelength (equivalent to 219 km for the control run) northeast, east, and southeast of the surface cyclone center (we chose locations downstream of cyclones since that is where deep convective storms tend to be most common and intense, and where the use of hodographs are most often employed; furthermore, at locations too near the center of the cyclone the model geostrophic winds are too weak, while at locations too

TABLE 2. Parameter values used in individual model configurations.

Variable (units)	"Control" value	Parameter range	Interval
a [K (1000 km)$^{-1}$]	10	2.5–22.5	2.5
L (km)	3500	2500–4500	250
λ (km)	$L/4$	0–$L/2$	$L/16$
$\hat{T}$ (K)	10	0–20	2.5
Φ_o (m^2 s^{-2})	1020	0–1020	127.5

far east of the cyclone center the model winds in the upper troposphere are affected by the anticyclonic flow associated with the downstream ridge) for the control and each parameter modulation, at a fixed time. Parameter ranges are shown in Table 2. This procedure generated 123 individual hodographs for analysis, valid for a wide spectrum of baroclinic wave intensities and configurations.

b. Aspects of the "control" configuration

An initial, "control" configuration was used to establish a baseline to compare to each parameter modulation, as described in the previous section. The "control" configuration represents moderately intense, westward sloping baroclinic waves configured such that the temperature field lags the 1000-mb height field by one-quarter wavelength (Fig. 2). This lag represents the most unstable phase lag consistent with baroclinic instability theory (Holton 1992) and leads to height-tendency fields indicative of a rapidly amplifying and intensifying wave throughout the lower to middle portions of the troposphere. There is a relatively strong baroclinic zone to

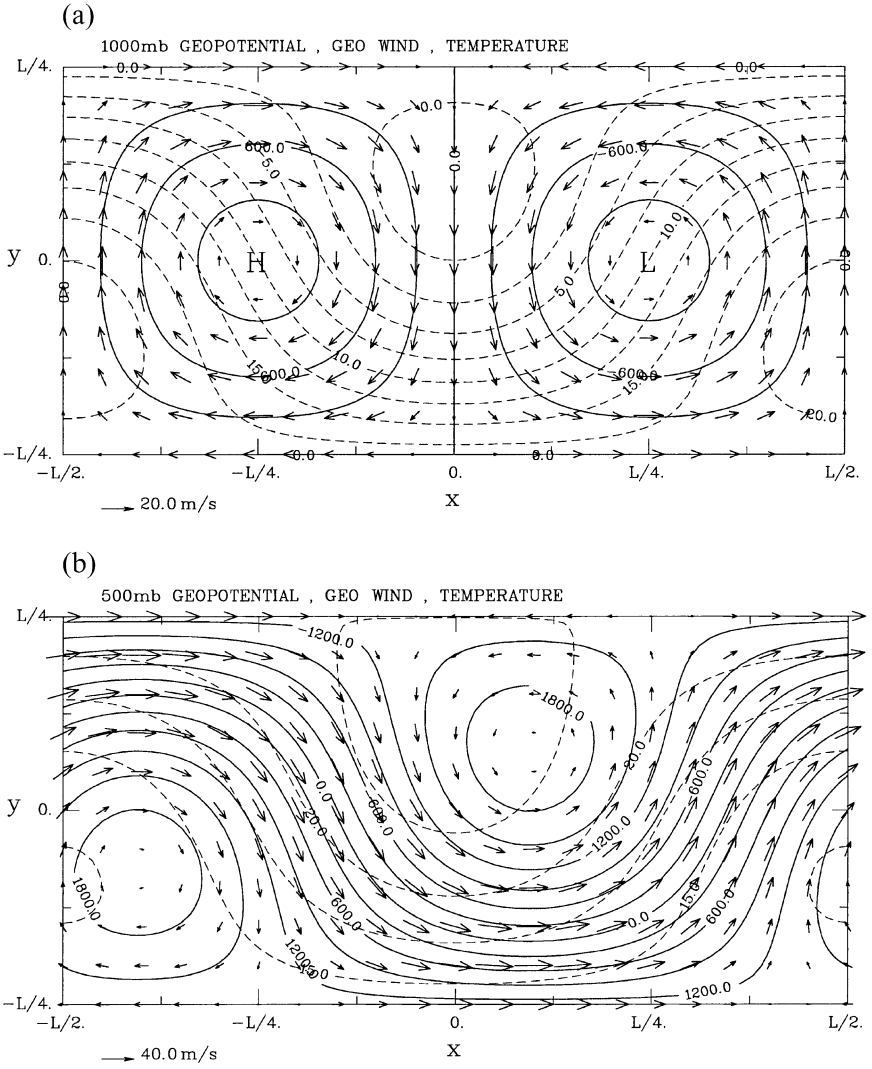

FIG. 2. Sanders' model "control" configuration. The (a) 1000- and (b) 500-mb geopotential (solid lines) and temperature fields (dashed lines) and geostrophic wind vectors. The (c) 1000- and (d) 500-mb height tendency field (negative values dashed) and isallohypsic wind vectors.

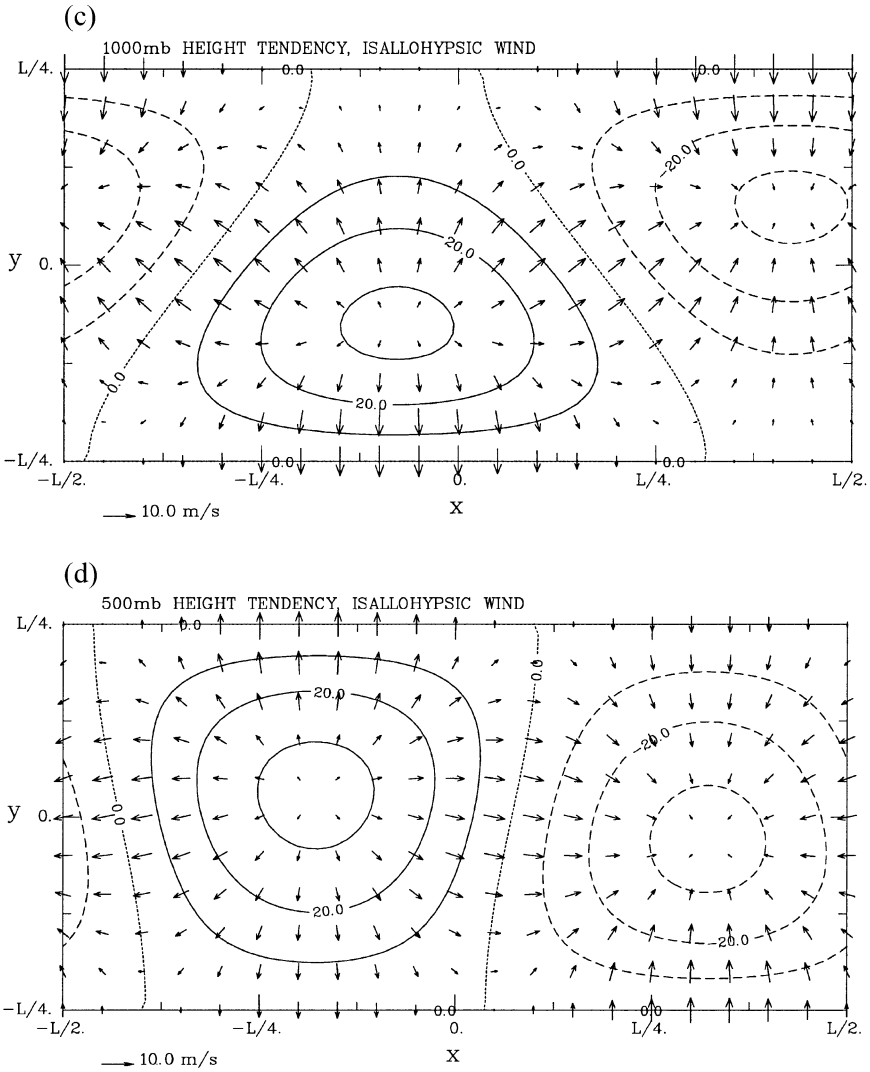

FIG. 2. (*Continued*) Isopleths of geopotential are given at intervals of 600 $m^2 s^{-2}$ and are plotted as the departure from the level average value. Isallohypses are labeled in units of 10^{-3} $m^2 s^{-3}$. Temperature is given in °C [values are negative in (b)].

the northeast and southwest of the surface low. Although the magnitude of the quasi-horizontal temperature gradient decreases with height, the isotherm *orientation* does not change with height. From the thermal-wind relationship, this implies that the geostrophic vertical shear in $\mathbf{v}_g$ must be entirely unidirectional in the model. In the atmosphere, straight hodographs in the mean are observed, to a first-order approximation, away from the tropopause and planetary boundary layer (PBL) (e.g., Fig. 5 of Bluestein and Banacos 2002). Minimal change in isotherm orientation with height is also often observed within frontogenetic deformation zones where narrow banded precipitation areas are sometimes found; however, there is not necessarily a physical constraint on the vertical parallelism of the quasi-horizontal temperature gradient. Thus, the model represents structures we observe in the real atmosphere; however, the domain of possible synoptic-scale wind field configurations associated with baroclinic waves cannot be fully encapsulated by the model mathematics because it requires simple analytic solutions. For example, if the height perturbation centers were allowed to vary in the meridional direction with height, and/or positive or negative tilts (with latitude) could be associated with the baroclinic systems, then some degree of curvature in the hodograph of the geostrophic wind would be possible. These synoptic configurations would likely need to be investigated numerically and are beyond the scope of this work.

Curvature in the hodograph of the total wind (i.e., geostrophic plus ageostrophic components) in the Sanders model must therefore be associated with the QG ageostrophic wind, and without the ''aid'' of friction since a boundary layer is not incorporated in the model.

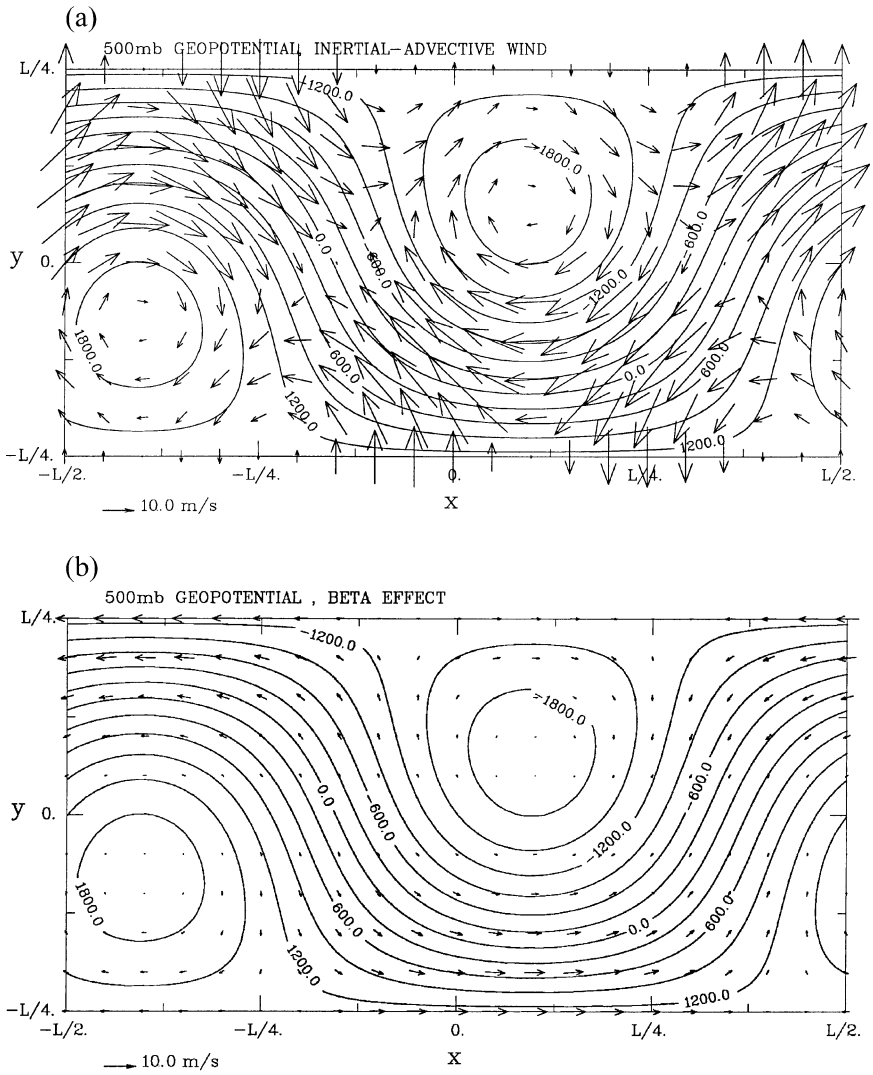

FIG. 3. Sanders' model ''control'' configuration. (a) The 500-mb geopotential field and inertial-advective wind vectors, and (b) the effect of β on the wind field. Geopotential values are plotted as the departure from the level average value. Units as in Fig. 2.

We have therefore, by default, focused the analysis on determining what aspects of the baroclinic wave result in a favorable ageostrophic shear profile such that curvature in the total-wind hodograph is produced.

As can be seen through subjective comparison of Fig. 2d to Fig. 3a, the isallohypsic wind, which points ''down'' the gradient of height tendency, acts opposite of the inertial-advective wind, which is directed perpendicular and to the left of the horizontal parcel acceleration, to the northeast and southwest of the minimum in height tendency field (southeast of the surface cyclone, in this case). Thus, it can be difficult to assess qualitatively the resultant magnitude of the ageostrophic wind simply by visual inspection. The inertial-advective wind at 1000 mb (not shown) is smaller than at higher elevations owing to generally smaller values of $|\mathbf{v}|$ and $|\nabla\mathbf{v}|$. The isallohypsic contribution to the ageostrophic wind does not vary appreciably with height in the control simulation; however, its magnitude relative to that of the inertial-advective wind is larger at low levels. At the surface, the geopotential tendency field is dominated by the effects of warm advection decreasing with height, for example, northeast of the surface cyclone, where a negative height tendency field (and deep-layer upward vertical motion) is maximized. In the midtroposphere, the height falls are largest east of the surface low, owing to the dominant effect of vorticity advection downstream of the 500-mb trough, and the reduction of temperature advection with decreasing pressure in the model.

This analysis aids in explaining the geostrophic, ageostrophic, and total-wind hodographs one-sixteenth of a wavelength northeast, east, and southeast of the surface low (Fig. 4). Although the hodograph of the

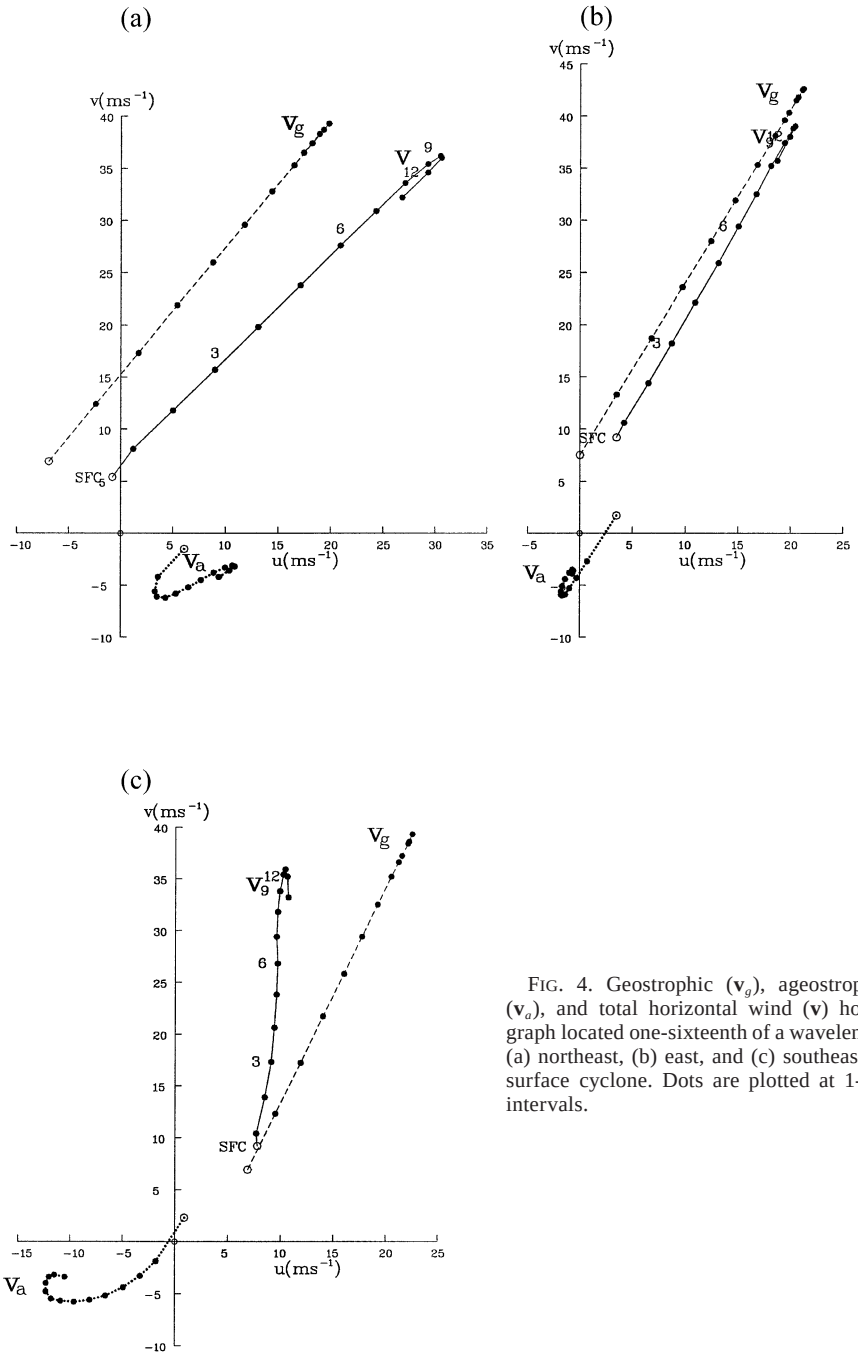

FIG. 4. Geostrophic ($\mathbf{v}_g$), ageostrophic ($\mathbf{v}_a$), and total horizontal wind ($\mathbf{v}$) hodograph located one-sixteenth of a wavelength (a) northeast, (b) east, and (c) southeast of surface cyclone. Dots are plotted at 1-km intervals.

geostrophic wind northeast of the low (Fig. 4a) is straight, there is still pronounced veering of the geostrophic wind with height, consistent with deep-layer warm advection. We see that the geostrophic shear weakens gradually with height (but much more rapidly above 7 km) and that the total-wind hodograph ''folds'' over onto itself at the tropopause where ∇T reverses direction, consistent with (2). It is noted in Fig. 4a that the ageostrophic wind veers through the 0–3-km AGL layer. This veering implies dominance of the isallohypsic contribution to the total ageostrophic wind in this layer, as veering of the isallohypsic wind component occurs northeast of the surface low from the low to midtroposphere following the vertical variation of the negative height tendency center as seen in Figs. 2c and 2d. Above 3 km AGL, the ageostrophic wind backs with height until the tropopause, increasingly affected by the northeastward-pointing inertial-advective wind downstream of the trough–ridge inflection point (Fig. 3a). This component becomes dominant over the isallohyp-

sic wind as wind speed and curvature effects increase with height. The reversal in temperature gradient above the tropopause yields an anticyclonic-turning ageostrophic wind hodograph between 10 and 13 km AGL and leads directly to the same turning in the total-wind hodograph. This turning at the tropopause was observed in composite mean hodographs in Bluestein and Banacos (2002; their Figs. 5 and 6), but was generally broader, suggesting a more gradual change in wind direction. This turning may be attributable to curvature in the hodograph of the geostrophic wind that does not occur in the model, or partly due to the ''smearing'' effect of averaging rawinsonde winds across varying tropopause heights in the observational composites.

East of the cyclone by one-sixteenth of a wavelength (Fig. 4b), the hodographs of the geostrophic and total wind are more backed aloft because the upper-level flow is more meridionally oriented, while exhibiting less veering owing to decreased warm temperature advection in the area. The ageostrophic wind component is weaker than the geostrophic wind component and weaker than the ageostrophic wind northeast of the cyclone; however, it also more directly opposes the geostrophic wind, owing to cyclonic flow aloft and a dominant inertial-advective contribution.

Of the three hodographs, the strongest ageostrophic wind component is found southeast of the cyclone (Fig. 4c) (approximately one-third of $|\mathbf{v}_g|$ at 10 km AGL), beneath the ''core'' of strongest upper flow and strong cyclonic curvature to the flow. The ageostrophic vertical shear vector opposes and points to the left of the geostrophic shear vector, contributing to the most backed hodograph of the total flow.

Below the tropopause, the model hodographs northeast and southeast of the surface low compare reasonably well with observations (i.e., Fig. 6 of Bluestein and Banacos, 2002), with the obvious exception of the absence of hodograph curvature in the PBL. Specifically, the vertical shear vector in the 3–8-km AGL layer is relatively unidirectional in the observational composites as it is in the model hodographs. In this layer the direction of the total wind shear vector in the observational composite is similar to that in the model to the northeast of the cyclone center; it, however, is directed more poleward in the model, southeast of the cyclone center, than is the climatological shear vector. In the strongest cyclones (Fig. 8 of Bluestein and Banacos 2002), a more poleward-directed midtropospheric shear vector is found to the southeast of the surface low, consistent with an upper trough of greater amplitude. Clearly, the direction of the deep tropospheric shear vector can vary from quadrant to quadrant around pressure systems, dependent largely upon the shape, wavelength, and amplitude of the upper wave.

c. Analysis of the Rossby number

An important consideration in the analysis of the resulting hodographs is that the Rossby number (Ro) associated with the large-scale flow field must be relatively small to be certain that quasigeostrophy is a valid assumption and therefore that our vertical shear solutions are valid. The Rossby number is defined as the ratio of the magnitude of the inertial acceleration to the magnitude of that induced by the Coriolis force (Bluestein 1992), which in our case simplifies as follows:

$$\mathrm{Ro} = \frac{\left|\dfrac{D\mathbf{v}}{Dt}\right|}{|f\mathbf{k} \times \mathbf{v}|} = \frac{|f\mathbf{k} \times \mathbf{v}_a|}{|f\mathbf{k} \times \mathbf{v}|} = \frac{|\mathbf{v}_a|}{|\mathbf{v}|}. \qquad (20)$$

For QG theory to be valid quantitatively, the magnitude of the inertial acceleration should be an order of magnitude less than that induced by the Coriolis force (i.e., Ro $\sim$ 0.1). The variation in Ro $L/16$ east of the surface cyclone for the ''control'' configuration of the Sanders model is shown in Figs. 5a–e. The greatest variation in Ro occurs at mid- and upper levels of the troposphere when the phase lag between the height and temperature fields is varied (Fig. 5b). The increasing magnitude of the inertial-advective wind (in a direction opposite the geostrophic wind) as the phase lag decreases causes an increasingly large Ro as the phase lag diminishes to 0. This increase in magnitude of the inertial-advective wind contributes to large fluctuations in the hodograph as phase lag is modified, as quantified in the next section of the paper.

As one might expect, a large variation in Ro also occurs for variations in the system wavelength (Fig. 5e): larger ageostrophic wind speeds relative to both total and geostrophic wind speeds are found as the wavelength is shortened. The Rossby number at low levels increases most rapidly to as great as 0.8 when $L = 2500$ km. Thus, wavelength may play a larger role in low-level hodograph curvature than the phase lag parameter.

No appreciable change in Rossby number occurs when the meridional temperature gradient is varied (Fig. 5a). Some change in Rossby number is observed when the surface geopotential perturbation is changed (Fig. 5c), but it remains relatively small (at or below 0.25). An increase in perturbation temperature (Fig. 5d) results in a general decrease in Ro, as the thermal-wind shear increases with little or no compensating change in ageostrophic wind.

d. Analysis of hodograph curvature and shear

With Ro in mind, we now examine hodograph curvature and the magnitude of the shear vector for each of the five variables across the parameter space shown in Table 2. The physical effects of hodograph curvature on convective storms are discussed in Weisman and Rotunno (2000) and Davies-Jones (2002).

Hodograph curvature was defined in terms of degrees of turning and was computed through depths of 0–2, 0–6, and 0–9 km AGL. The magnitude of the shear vector was also measured through these layers. Since

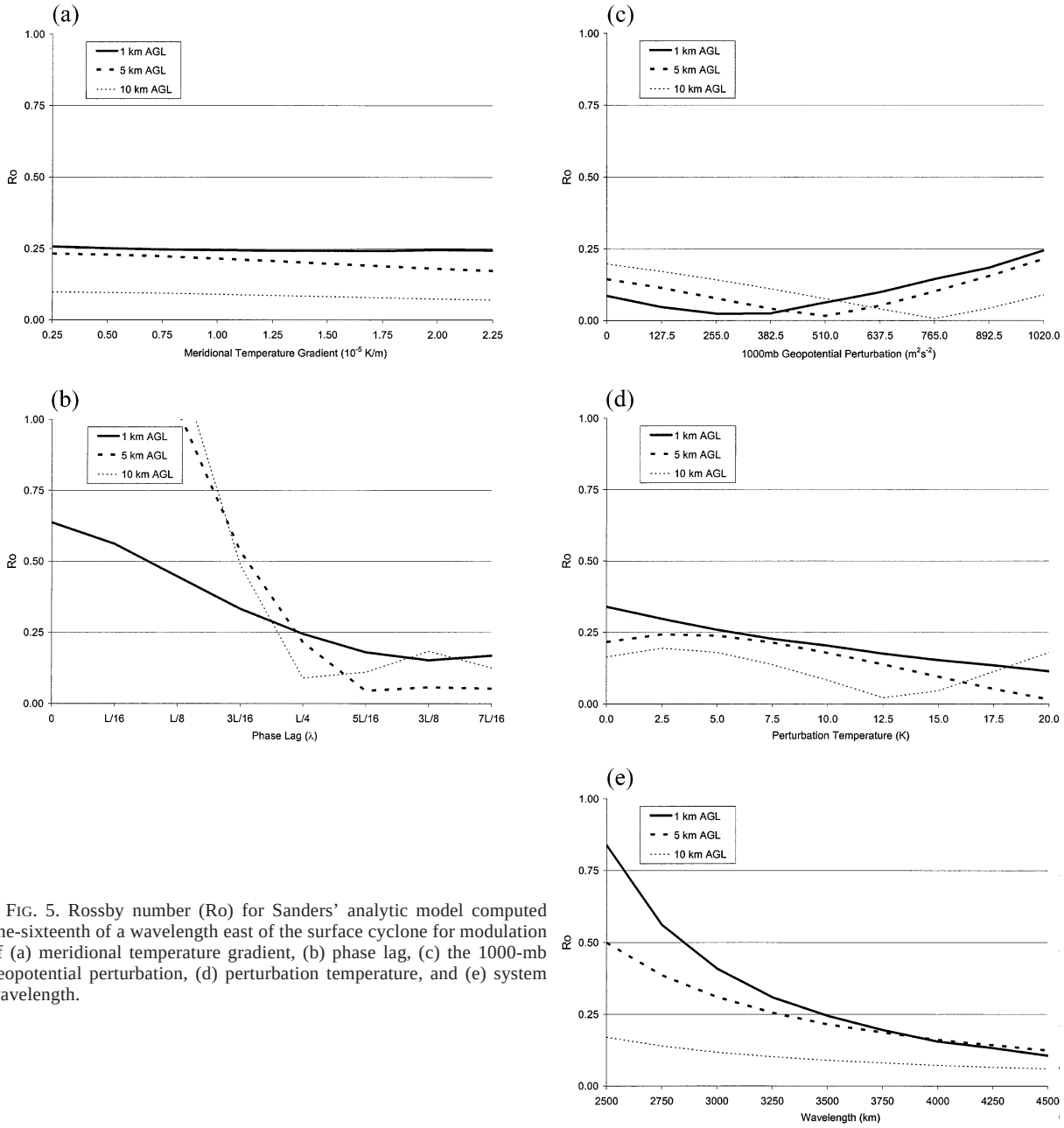

FIG. 5. Rossby number (Ro) for Sanders' analytic model computed one-sixteenth of a wavelength east of the surface cyclone for modulation of (a) meridional temperature gradient, (b) phase lag, (c) the 1000-mb geopotential perturbation, (d) perturbation temperature, and (e) system wavelength.

large curvature values in shallow layers in the presence of weak deep-layer shear generally do not contribute appreciably to the organization or longevity of convective storms, the curvature values are analyzed in conjunction with the magnitude of the 0–6-km shear vector. In the discussion that follows, we refer to deep-layer shear as the magnitude of the shear vector in the 0–6-km layer or greater, consistent with operational usage of the terminology. The distribution of hodograph curvature (clockwise turning with height is positive; counterclockwise turning with height is negative) and 0–6-km shear is shown for each of the five synoptic variables in Figs. 6a–e.

Deep-layer shear varies as the meridional temperature gradient (Fig. 6a), according to the thermal-wind relation. However, the turning in the hodograph remains essentially unchanged throughout the parameter space and is minimal.

Phase lag (Fig. 6b) produces a large variability in both hodograph turning and deep-layer shear since a change in the juxtaposition of the height and temperature distribution through the troposphere has a significant impact on height gradient and the resulting magnitude of the geostrophic wind. The geostrophic, ageostrophic, and total-wind hodographs for modulation of phase lag are displayed in Figs. 7a–h to allow the reader

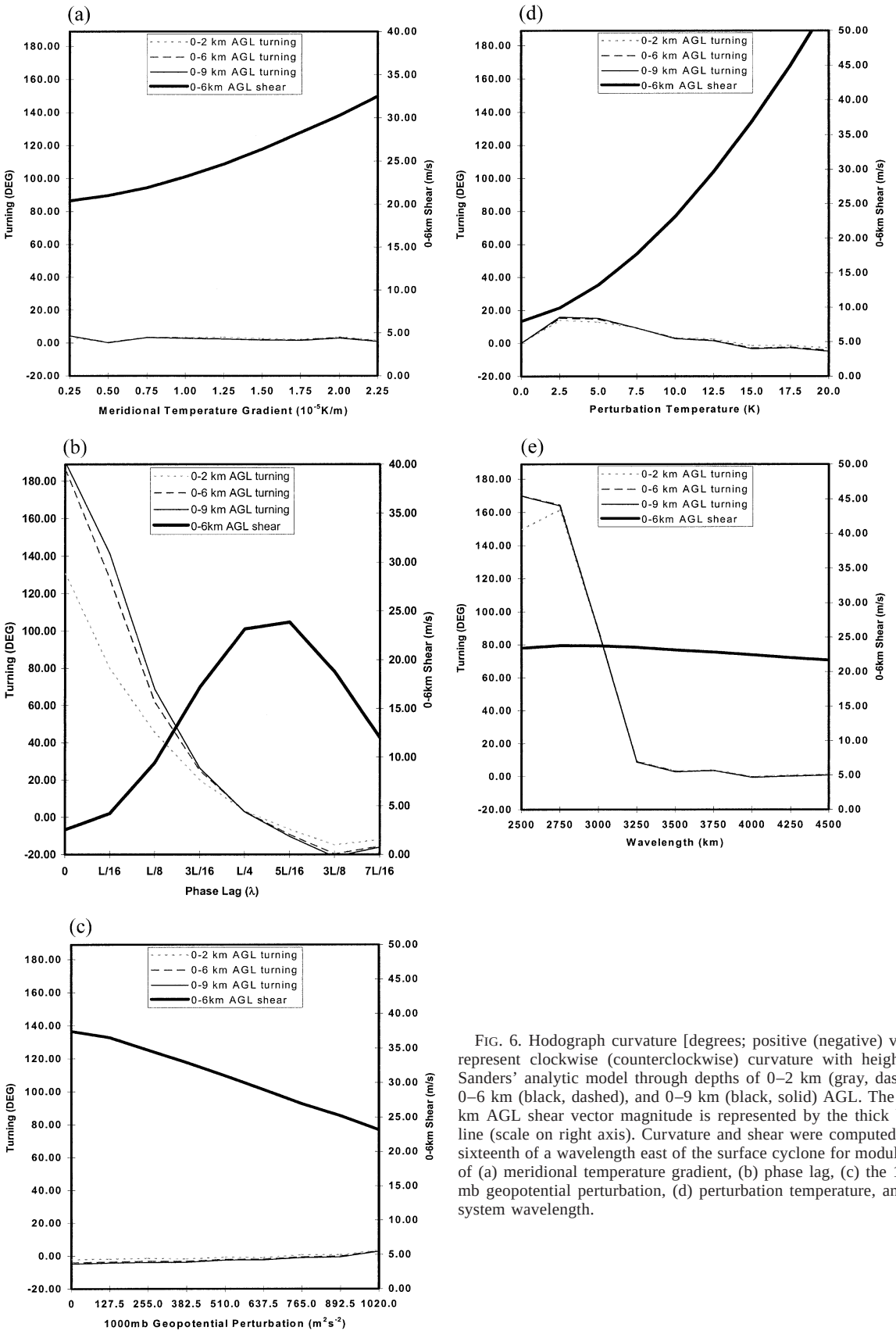

FIG. 6. Hodograph curvature [degrees; positive (negative) values represent clockwise (counterclockwise) curvature with height] in Sanders' analytic model through depths of 0–2 km (gray, dashed), 0–6 km (black, dashed), and 0–9 km (black, solid) AGL. The 0–6-km AGL shear vector magnitude is represented by the thick black line (scale on right axis). Curvature and shear were computed one-sixteenth of a wavelength east of the surface cyclone for modulation of (a) meridional temperature gradient, (b) phase lag, (c) the 1000-mb geopotential perturbation, (d) perturbation temperature, and (e) system wavelength.

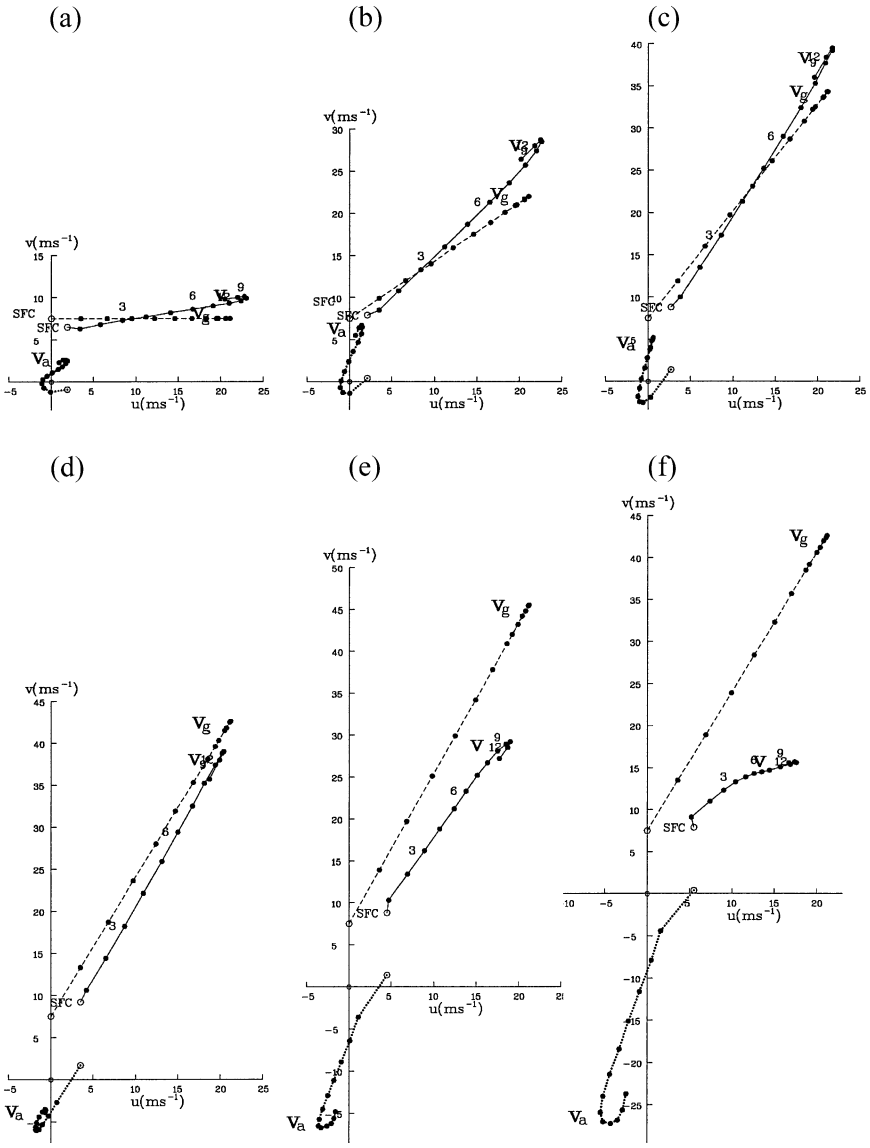

FIG. 7. As in Fig. 4, but for phase lag values of (a) 7*L*/16, (b) 3*L*/8, (c) 5*L*/16, (d) *L*/4, (e) 3*L*/16, (f) *L*/8,

to visualize better the influence of this parameter and as an aid in the interpretation of Fig. 6b. The greatest low-level turning (~10°) for values of 0–6-km shear in excess of 20 m s^{-1} occurs around 7*L*/32. There is much greater turning at lower phase lag; however, there is considerably less deep-layer shear at these values of phase lag. ''Supercell'' shear (i.e., greater than 20 m s^{-1} over the lowest 6 km) is found from $\lambda \sim 7L/32$ to just under 3*L*/8.

Changes in the 1000-mb geopotential height perturbation (Fig. 6c) result in a negligible change in hodograph turning; the hodograph is nearly straight throughout the parameter space. The shear from 0–6 km decreases with increasing 1000-mb geopotential height perturbation. This decrease is related to the direct relationship between the 1000-mb height gradient and surface $\mathbf{v}_g$, with a decrease in shear as surface $\mathbf{v}_g$ increases.

Some variability in hodograph turning (up to ~18°) is observed for relatively small values of perturbation temperature (Fig. 6d), but it tends to occur at very low (nonsupercellular) values of 0–6-km shear (less than 20 m s^{-1}).

Modulation of system wavelength (Fig. 6e) produces little change in 0–6-km shear, which remains between 22 and 24 m s^{-1} throughout the parameter space. However, a very large and abrupt increase in hodograph turning is observed as the system wavelength is shortened from 3250 to 3000 km. This turning at short wavelengths is very marked. The nearly identical magnitude of turning through all three layers for the system wave-

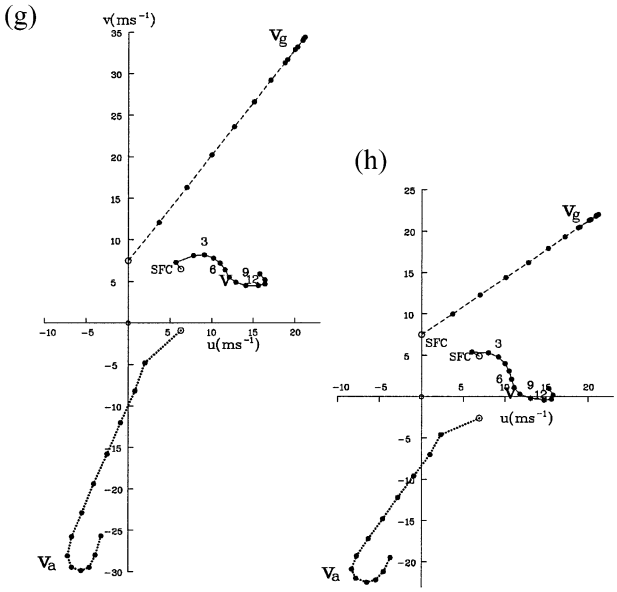

FIG. 7. (*Continued*) (g) *L*/16, and (h) 0 at a location one-sixteenth of a wavelength east of the surface low.

length parameter space implies that nearly all the turning occurs in the 0–2-km layer. The low-level (1 km) *Ro* associated with flow between 3000 and 3250 km at this point in the cyclone is 0.3–0.4, suggesting QG theory is still reasonably valid. Examination of the low-level isallohypsic field (not shown) indicates that this increase is attributed to much larger low-level height tendency gradients and isallohypsic wind components. It is also worth noting that, consistent with the Rossby wave speed equation, troughs of shorter (longer) wavelength exhibit a faster (slower) downstream propagation. We therefore expect short-wave troughs having a wavelength shorter than 3250 km, or relatively fast moving troughs, to be associated with a greater potential for large low-level turning or curvature in the hodograph, particularly when the phase lag is near 7*L*/32 (at which the greatest low-level turning occurs with the 0–6-km shear in excess of 20 m s^{-1}, i.e., when the hodograph is like that associated with supercells). This finding may help explain operational experience suggesting that potential tornado outbreaks are ''favored'' by faster moving short-wave troughs (S. Weiss 2003, personal communication).

The impact of the meridional temperature gradient, the 1000-mb geopotential height perturbation, and the perturbation temperature on hodograph curvature is minimal. However, modulation of these parameters strongly influences the magnitude of deep-layer shear.

4. Concluding discussion and future work

We focused here on how the variations of five synoptic-scale parameters specific to Sanders' model affect the hodograph shape and curvature and how the magnitude and character of the geostrophic and ageostrophic wind (decomposed into the inertial-advective and isallohypsic components) contribute to the vertical variation of horizontal wind. It was found that system wavelength and phase lag made the largest contribution to hodograph turning when 0–6-km shear supportive of supercells (greater than 20 m s^{-1}) is present. Hodograph curvature in general is most favored by short wavelength systems and augmented by small phase lag.

There are, of course, an infinite number of synoptic-scale baroclinic wave configurations that are possible in the model. The authors believe that the concept of an ''ideal'' synoptic-scale baroclinic wave structure for specific atmospheric processes, where attributes of the *local* wind field are essential to the existence of a specific event, is worthy of further investigation in either observational studies or more complex numerical model simulations. The pattern recognition aspect of this approach is potentially helpful in increasing situational awareness of operational forecasters and in highlighting the importance of atmospheric-scale interactions. Use of a numerical model to do the same type of analysis would be needed to consider more accurately some effects such as friction in the PBL and variations of the temperature perturbation centers when they are not at the same latitude as that of the surface pressure centers. Balance models of higher order would also more realistically represent the ageostrophic wind, which may affect the resulting degree of hodograph curvature. An observational study of hodographs with specific reference to the geostrophic and ageostrophic parts of the wind that goes beyond the climatology of Bluestein and Banacos (2002), classified with specific regard to measured large-scale parameters (such as those used in Sanders' model), would be useful to better understand the synoptic-scale influences on the wind field in close proximity to where convective storms develop.

Acknowledgments. The authors thank Fred Carr (OU) and Mike Richman (OU) for sharing their ideas and for serving on the first author's M.S. thesis committee; the first author's thesis, in part, formed the foundation for this paper. This research was supported by NSF Grant ATM-9612674 and-9912097 and the School of Meteorology at OU. Additional analysis and research was performed at the Storm Prediction Center (SPC). Joe Schaefer, Russ Schneider, and Steve Weiss, all of the SPC, are acknowledged for their support and discussions relating to this project.

REFERENCES

Banacos, P. C., 1999: The wind and thermal structure surrounding synoptic-scale cyclones and anticyclones over the eastern two-thirds of the United States: A climatological analysis. M.S. thesis, School of Meteorology, University of Oklahoma, 221 pp. [Available from School of Meteorology, University of Oklahoma, 100 E. Boyd, Rm. 1310, Norman, OK 73019.]

Bluestein, H. B., 1992: *Principles of Kinematics and Dynamics,* Vol.

I, *Synoptic-Dynamic Meteorology in Midlatitudes*. Oxford University Press, 431 pp.
——, 1993: *Observations and Theory of Weather Systems*, Vol. II, *Synoptic-Dynamic Meteorology in Midlatitudes*. Oxford University Press, 594 pp.
——, and M. H. Jain, 1985: Formation of mesoscale lines of precipitation: Severe squall lines in Oklahoma during the spring. *J. Atmos. Sci.*, **42,** 1711–1732.
——, and M. L. Weisman, 2000: The interaction of numerically simulated supercells initiated along lines. *Mon. Wea. Rev.*, **128,** 3128–3149.
——, and P. C. Banacos, 2002: The vertical profile of wind and temperature in cyclones and anticyclones over the eastern two-thirds of the United States: A climatology. *Mon. Wea. Rev.*, **130,** 477–506.
Brooks, H. E., C. A. Doswell III, and R. B. Wilhelmson, 1994: The role of midtropospheric winds in the evolution and maintenance of low-level mesocyclones. *Mon. Wea. Rev.*, **122,** 126–136.
COESA, 1976: *U.S. Standard Atmosphere*. NOAA, 227 pp.
Davies-Jones, R., 2002: Linear and nonlinear propagation of supercell storms. *J. Atmos. Sci.*, **59,** 3178–3205.
Glickman, T. S., N. J. Macdonald, and F. Sanders, 1977: New findings on the apparent relationship between convective activity and the shape of 500 mb troughs. *Mon. Wea. Rev.*, **105,** 1060–1061.
Holton, J. R., 1992: *An Introduction to Dynamic Meteorology*. Academic Press, 511 pp.
Macdonald, N. J., 1976: On the apparent relationship between convective activity and the shape of 500 mb troughs. *Mon. Wea. Rev.*, **104,** 1618–1622.
Maddox, R. A., 1976: An evaluation of tornado proximity wind and stability data. *Mon. Wea. Rev.*, **104,** 133–142.
Rasmussen, E. N., and J. M. Straka, 1998: Variation in supercell morphology. Part I: Observations of the role of upper-level storm-relative flow. *Mon. Wea. Rev.*, **126,** 2406–2421.
Sanders, F., 1971: Analytic solutions of the non-linear omega and vorticity equation for a structurally simple model of disturbances in the baroclinic westerlies. *Mon. Wea. Rev.*, **99,** 393–407.
Weisman, M. L., and J. B. Klemp, 1982: The dependence of numerically simulated convective storms on vertical wind shear and buoyancy. *Mon. Wea. Rev.*, **110,** 504–520.
——, and ——, 1984: The structure and classification of numerically simulated convective storms in directionally varying wind shears. *Mon. Wea. Rev.*, **112,** 2479–2498.
——, and R. Rotunno, 2000: The use of vertical wind shear versus helicity in interpreting supercell dynamics. *J. Atmos. Sci.*, **57,** 1452–1472.